Eur. Phys. J. Spec. Top. (2022) 231:4185–4193
https://doi.org/10.1140/epjs/s11734-022-00573-y

THE EUROPEAN PHYSICAL JOURNAL SPECIAL TOPICS

Regular Article

Microstructural features and piezoelectric properties of spark plasma sintered lead-free $K_{0.5}Na_{0.5}NbO_3$ ceramics

Isabelle Monot-Laffez[1,a], Richard Retoux[2], Mustapha Zaghrioui[1], Micka Bah[1], Marion Dubernet[1], Frédéric Dorvaux[1], Fabian Delorme[3], and Fabien Giovannelli[1]

[1] GREMAN Laboratory, UMR 7347, University of Tours, CNRS, INSA CVL, 37200 Tours, France
[2] CRISMAT Laboratory, UMR6508, Normandie University, ENSICAEN, UNICAEN, CNRS, 14050 Caen, France
[3] *Present Address*: ISL, French-German Research Institute of Saint-Louis, 68301 Saint-Louis Cedex, France

Received 28 January 2022 / Accepted 9 April 2022 / Published online 27 April 2022

Abstract To replace lead containing (Pb, Zr)TiO_3 in piezoelectric devices, the (K, Na)NbO_3 system has shown great promise but has also encountered versatile properties, due to the volatilization of alkaline elements and difficulties in getting fully dense ceramics. $K_{0.5}Na_{0.5}O_3$ (KNN) powders are prepared by solid-state synthesis with a short-time planetary ball milling and shaped in a series of ceramic pellets using spark plasma sintering technique (SPS), resulting in highly dense ceramics. This sintering process operates in reducing conditions, and post-annealing in oxygen flow is required to recover a good electrical insulator material, to remove the residual strains in the ceramics and to eliminate possible carbon contamination from the graphite die. The structural and microstructural states of the ceramics, observed before and after post treatment, lead to the identification of the major defects encountered during SPS treatment. The resulting piezoelectric functional properties obtained on the series of pellets after oxygen annealing post treatment are measured. This study confirms that SPS technique is really successful in achieving very high and reproducible densification of KNN ceramics. After a post-annealing treatment, substantial piezoelectric properties improvement can be expected in such high densification and defect-free ceramics, suitable for integration in lead-free devices.

1 Introduction

Piezoelectric materials are widely used for domestic, medical and industrial applications in industry as actuators, sensors, transducers and in other electromechanical devices. Thanks to their excellent and tunable piezoelectric properties, lead zirconate titanate (PZT)-based piezoceramics exhibiting a perovskite structure, discovered in 1954, have dominated the electronic device market worldwide [1].

However, the lead contained in these materials is a real issue because of its high toxicity for human health and environment, which lead to its prohibition by the European Union in 2003 [2]. The successive derogations from the RoHS and REACH directives granted to lead-containing materials (PZT), widely used in many piezoelectric and electronic applications, are coming to an end. There is an urgent need today to offer alternative materials to replace these compounds [3]. Since 2003, many works focused on the search and development of new lead-free piezoelectric materials for practical and target applications [4]. Today, a few new lead-free systems emerges, and concern BT (Ba–Ti–O), BNT (Bi–Na–Ti–O), BT (Bi–Ti–O), BFO (Bi–Fe–O), and KNN (K–Na–Nb–O), all of them of perovskite structure, although some weak toxicity remains in some of them [5–8].

Among these new candidates for piezoelectric devices, the sodium and potassium niobate (KNN) system seems to be one of the most interesting alternatives because of its high Curie (above 400°C) and T–O–T temperatures, low theoretical density, with rather high piezoelectric properties in ceramics, crystals and textured materials [9–15]. But these ceramics have to be further optimized for their integration in mass production of devices like transducers. Since Saito et al. published very high piezoelectric performances obtained for textured KNN ceramics doped with lithium, tantalum and antimony of global composition (Li, Na, K) (Nb ,Ta, Sb) O_3 [16], an abundant literature followed, and many results of this composition were published [17,18]. Li, Mn, CuO, Sr, Zr, Ti, Co or Ta doping or co-doping [17,19–26] was reported as improving the piezoelectric charge coefficient d_{33} (pC/N or pm/V), which quantifies the volume change when a piezoelectric material is subjected to an electric field or the polarization on application of a stress. For transducer applications, the necessity to produce thick and dense ceramics with good electromechanical coupling is needed [27,28].

[a] e-mail: isabelle.laffez@univ-tours.fr (corresponding author)

Many studies were based on complex substitutions to improve properties through creating new phase boundaries and coexisting structures [6,29].

However, the KNN system is often considered in the literature as easily non-stoichiometric because of alkali volatilization and very difficult to sinter because of a strong competition between grain growth (Oswald ripening easily occurs in this system) and densification [30] . As a reminder, previous results have shown that conventional undoped KNN sintering is usually handled at 1110–1140 °C for 2–10-h dwell time, and the final relative density is about 90–92% for the best [12,13,31] .

A few years ago, this issue could be knocked down with the possibility to use spark plasma sintering to densify the ceramics [32–35].

This technique, combining high-pulsed DC current, flowing through a carbon die and uniaxial pressure of several tens of mega Pascals, is used in this study to sinter KNN ceramics because it has been shown as an effective way to get high relative densities; the benefits of this technique are that lower temperatures and shorter time can be used compared to conventional sintering, and then alkali volatilization of K and Na encountered in KNN system can be greatly reduced due to confined conditions for the powder, embedded in the die. However, inert atmosphere (vacuum or Argon) is necessary to prevent carbon dies' collapse. Thus, there are some possible drawbacks with this technique, due first to the carbon graphite that can diffuse and contaminate the ceramics [36,37], and second some oxygen losses can occur in the oxide because of the reductive conditions [38]. Moreover, it has been shown that the densification occurs in a different way than with conventional sintering, with different diffusion mechanisms of the species due to the flowing current, and also the addition of creep phenomenon introduced by the pressure in the global equation: consolidation vs grain growth vs densification [39,40]. As a result, the microstructure can be very different, as well as the defects generated during the SPS process. The density of defects points defects, dislocations or non-stoichiometry might sensitively influence electrical conductivity and the domains mobility, and consequently the piezoelectric properties, as suggested in only few studies of KNN system [41–43].

To consider further applications based on KNN ceramics, it is necessary to carefully determine the influence of SPS conditions in three points: (i) the resulting microstructure, defects and/or oxygen vacancies that can be produced by SPS conditions, (ii) the possible carbon contamination by the graphite dies, and (iii) the effectiveness of the post annealing to recover an insulating, homogeneous and stable material under poling.

Thus, the observation and characterization of the crystallinity and the defects on KNN ceramics sintered by SPS are a practically virgin field of investigation. This is the subject of the present study for the understanding and the correlation between microstructure, defects and electrical / piezoelectric properties in KNN-based ceramics.

2 Materials and methods

2.1 Samples preparation

KNN powders are prepared by the conventional solid-state synthesis. Oxide and carbonate powders of K_2CO_3 (99+%, ChemPUR), Na_2CO_3 (99.9+%, ChemPUR), Nb_2O_5 (99.9%, ChemPUR, monoclinic) are used as starting materials. The raw powders are first dried at 300°C during 3 h, weighed in stoichiometric ratios and then mixed during 15 min at 300 rpm with planetary ball milling in agate mortar and balls. The resulting mixtures are calcined twice at 830°C for 5 h in dense alumina crucible with an intermediate grinding in the same conditions. After calcinations, the phases and grains size distribution are controlled. A series of ten dense ceramic pellets are then shaped using spark plasma sintering technique in a SPS Syntex 632Lx (FUJI) equipment. For each sample, 1.5 g of calcined powders is inserted in a 15 mm diameter graphite die with protective carbon foil and placed between two graphite punches in contact with electrodes. The system is then submitted to a heating cycle generated with pulse DC current, combined with a uniaxial pressure applied on the graphite punches with a programmed cycle. The whole system is working under Argon atmosphere to protect the carbon materials. Several sintering parameters were optimized, heating rates (50–100°C/min), dwell temperatures (920–980°C), dwell times (5–10 min), and pressure conditions (50–200 MPa). After spark plasma sintering, the samples are annealed under oxygen flow at 300°C/h from room temperature to 600°C and then 50°C/h from 600 to 900°C, followed by a dwell of 2h at 900°C, and controlled by complementary DTA–TGA analyses; the cooling rate is fixed at 300°C/h. All the pellets are then polished to obtain a thickness of 1mm with parallel surfaces for further characterizations and piezoelectric functional properties measurements.

2.2 Characterizations

Phase identification of the ceramics is carried out by X-ray diffraction with a Cu-Kα radiation filtered by Ni (BRUKER D8 X-Ray diffractometer) equipped with a high-performance linear detector, between 20° and 80° , with a 0.02° step and 1-s exposition time, equivalent to 192 s for a point detector.

The grain size distribution of the powders is controlled by beam laser granulometry (Horiba LA950) equipped with two wavelength lasers, 465nm and 650nm, to cover a wide range of grain sizes, from 0.4 to 200 microns.

DTA–TGA measurements are performed on a NETZSCH (STA2500 regulus) using platinum crucible. The runs are performed at 10°C/min up to 900°C, in air with 3-h dwell time.

UV–visible diffuse reflectance measurements were performed, on polished samples, from 200 to 900 nm using double-beam Jasco V-750 spectrometer, equipped

with an integrating sphere. $BaSO_4$ powder was used as a reference standard.

The measured diffuse reflectance, R, was converted in the Kubelka–Munk function, F(R), which is proportional to the absorption coefficient [44]. Optical gap energy is, thus, extracted from the Tauc plot, corresponding to the plot of $[F(R)xE]^n$ versus energy, E.

Raman and photoluminescence spectra were performed at room temperature on sintered samples surfaces using Renishaw Invia spectrometer in backscattering configuration. A 514 nm argon laser is used as an excitation with a power of 1 mW focused by X 50 lens.

The relative densities of the different ceramic pellets are measured by geometrical and weight measurements, and also Archimedes measurements, referred then to the theoretical density. Microstructure and compositions are checked, with a field gun emission scanning electron microscope (TESCAN-MIRA 3 SEM) coupled with energy-dispersive X-ray spectroscopy analysis (EDS—Oxford Inca Xact).

Due to low energy of oxygen, its quantification is very much challenging; the EDX quantification of elements is measured and calculated only on the cations.

The high-resolution transmission electron microscopy observations were performed at room temperature using an ARM200F cold FEG microscope operated at 200 kV and equipped with large solid angle CENTURIO EDX detector, Orius CCD camera. For TEM observations, the KNN ceramics were slightly crushed and deposited with alcohol on sample holder.

To perform electrical measurements, high-purity silver paint (SPI supplier) is pasted uniformly on both sides of the pellets and fired at 750° C for 30 min for the adhesion of the electrodes. All samples are then poled at 130°C in oil under 3 kV/mm for 10 min using a DC power supply and field cooled to room temperature. The complex electrical impedance is then measured according to frequency, using a Vector Network Analyzer (Omicron Lab Bode 100) under free piezoelectric resonator conditions. KLM equivalent electrical circuit [45,46] was employed to compute the theoretical behavior of the electrical impedance around the fundamental thickness resonance mode. With geometrical characteristics such as the upper electrode area, the ceramic thickness and density, a fit of the experimental impedance allows the identification of the different parameters: thickness coupling factor k_t, relative permittivity at constant strain ε^S_{33r}, and the quality factor Q_m, respectively. The planar coupling factor k_p is calculated by the resonance–antiresonance method on the basis of IEEE standards on Piezoelectricity [47].

3 Results and discussion

3.1 Macrostructure

The ten sintered pellets obtained from synthesized KNN powders result in relative density over 96% and up to 99%. This confirms that spark plasma sintering technique is really successful in reaching very high and reproducible densification of KNN ceramics. Thus, substantially piezoelectric properties improvement can be expected with such high relative densities but as shown in Fig. 1, all the samples come out from SPS with a dark blue–dark gray color, different from the usual white color of insulting KNN powders or ceramics. This dark color has been already described in several studies and post-annealing treatment is always mentioned in spark plasma sintered KNN [33,48–50]. This sample darkness can be due to oxygen losses coming from reductive conditions of SPS or due to carbon contamination. To address the first hypothesis, conductivity as low as 120 S/m at 1000 K was measured just after SPS process [51]. This is the signature of the existence of few conductive species that can be logically related to oxygen vacancies, but not in a large proportion, because the conduction drops to low conductivity, as low as 6 S/m at 350 K. This value is very low but does not correspond to a perfect insulator, and this can indicate the presence of oxygen vacancies

To go further, a difference of darkness is systematically observed between the two faces of the sample. considering the reductive conditions coupled with the pulse DC current applied always in the same direction (as shown in Fig. 1, from top to bottom sides). The formation of oxygen vacancies during sintering, under reductive conditions, can be expressed as:

$$O_O^X \rightarrow 1/2O_2 \uparrow + V_O^{\cdot\cdot} + 2e^{'}. \quad (1)$$

The transformation of an oxygen in the structure into oxygen gas is accompanied by the formation of a positive oxygen vacancy and two electrons. The experimental conditions favor the migration of oxygen vacancies only in one direction (from top to bottom sides) and result in a more deoxygenated bottom side than the upper one, and thus appearing with in a darker color than the top face, as shown in Fig. 1. The free electrons generated can be trapped by Nb^{5+} ion which can reduce its valence, as already suggested [52]. They are also responsible of the low electrical conductivity described above.

To confirm the possibility to recover full oxygen by thermal post-treatment and also to consider the second point about a possible carbon contamination coming from the carbon materials, an oxygen treatment was followed by DTA-TGA analysis (Fig. 2).

Crushed parts of raw KNN ceramics, just after SPS sintering, were annealed in oxygen up to 900°C, followed by 3 hours dwell time. First of all, DTA curve clearly indicates the structural transition encountered in pure KNN with the Orthorhombic to Tetragonal transition T–O–T occurring at 194°C and the Curie temperature T_C detected at 415°C, in accordance with the common results on KNN (3). The thermogravimetric line in Fig. 2 indicates a mass loss of 0.8 wt% between 20 and 600 °C. This can be attributed to carbon or carbonates decontamination and more proba-

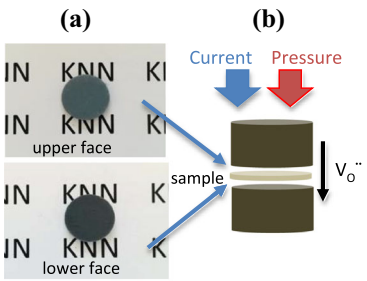

Fig. 1 **a** Systematic difference of the samples color observed between upper and lower surface, after extraction from the SPS die, and polishing of the surface to remove the contact surface with carbon foil. **b** Schematic application of pressure and current to illustrate a possible oxygen migration

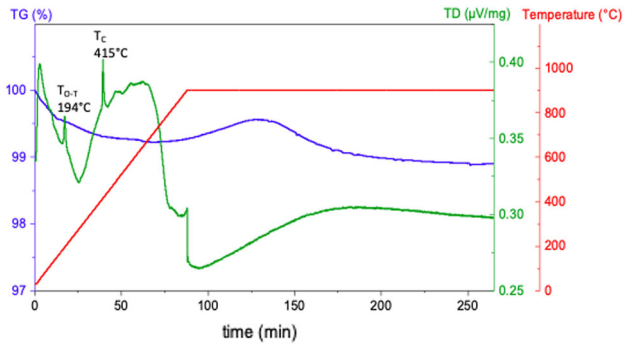

Fig. 2 Thermogravimetric analysis of oxygen annealing of raw SPS ceramics, up to 900°C at 10°C/min followed by 3 h dwell

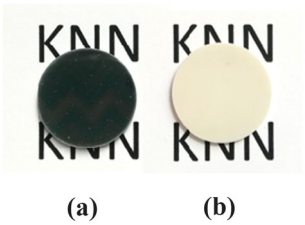

Fig. 3 Color of **a** the raw SPS ceramic and **b** after oxygen post-treatment, with the recovered white milky color of KNN

bly water dehydration in this temperature range, as frequently encountered in oxides. This step is immediately followed by a mass gain of about 0.35% up to 900°C. This latter can be attributed to oxygen uptake which diffusion rate is good in this temperature range, reduced by carbon decontamination occurring during all the heating step. After less than one hours at 900°C, no more uptake is observed and a longer time indicates a slight loss of weight. From these considerations, a post annealing treatment under oxygen flow up to 900°C, with one-hour dwell has been successfully implemented on the raw SPS KNN pellets. A complete recover of the white milky color of KNN is always obtained, as illustrated in Fig. 3.

3.2 Structure and microstructure

SEM microstructures of KNN powders and SPS ceramics sintered at 920°C for 10 min, under 50 MPa are shown in Fig. 4. The synthesized powder exhibits a rather regular cubic shape with a mean grain size of 3 microns spreading from 0.3 to 5 microns (Fig. 4a), confirmed by laser granulometry in water (with Fraunhofer model). The in-beam SE images are sensitive to the topological defects and the surface state of the grains, and it is clearly shown that the grains have no evidence of strains, cracks, neither surface roughness nor sharp angles.

The powders quality is confirmed by XRD in Fig. 5a which shows only peaks of pure orthorhombic structure corresponding to PDF card 04-017-0216 of $K_{0.5}Na_{0.5}NbO_3$. In the same way, a sharp contrast without defects in the majority of the grains is observed by high-resolution electron microscopy (Fig. 5b). In some rare grains, typical disturbed contrast is evidenced, confirming the existence of localized lower crystallized areas in the grains. These disturb contrasts are the consequence of local composition heterogeneities or due to the presence of a certain densities of defects in the grains (only a few % in volume). However, it does not represent the main tendency of the samples and attests the good crystallinity of the synthesized powders. EDX analysis indicates a cationic composition close to the expected one of $K_{0.5}N_{0.5}Nb_{1.0}O_x$ within the 2% accuracy of this quantification.

As a partial conclusion for the powders, the synthesized KNN obtained by solid-state process and rather short time planetary ball milling compared to other studies are X-Ray diffraction pure, highly crystallized with low defects. These precursor powders are suitable to study their sintering by spark plasma sintering and to study the influence of this process on the defects structure in the resulting ceramics.

After sintering a full dense microstructure is obtained with a slightly bigger mean grain size of 5–6 microns calculated from 100 measured grains from SEM microstructures (Fig. 4b, c). Their sizes spread between 2 and 10 microns, with facetted cuboid grains highly packed and thin grain boundaries. The geometrical and Archimedes relative densities are between 97 and 99% for the batch of ten measured pellets. In spite of a strong competition between densification and grain growth, this latter can be limited, thanks to the short time at high temperature and the pressure of tens of MPa applied all along the heating process. These are also conditions to reduce the volatility of the alkali elements and keep the stoichiometry.

3.3 Defects analysis

To further investigate the possible defects introduced during the SPS process, TEM observations on slightly crushed ceramics were conducted and the results are summarized in Fig. 6.

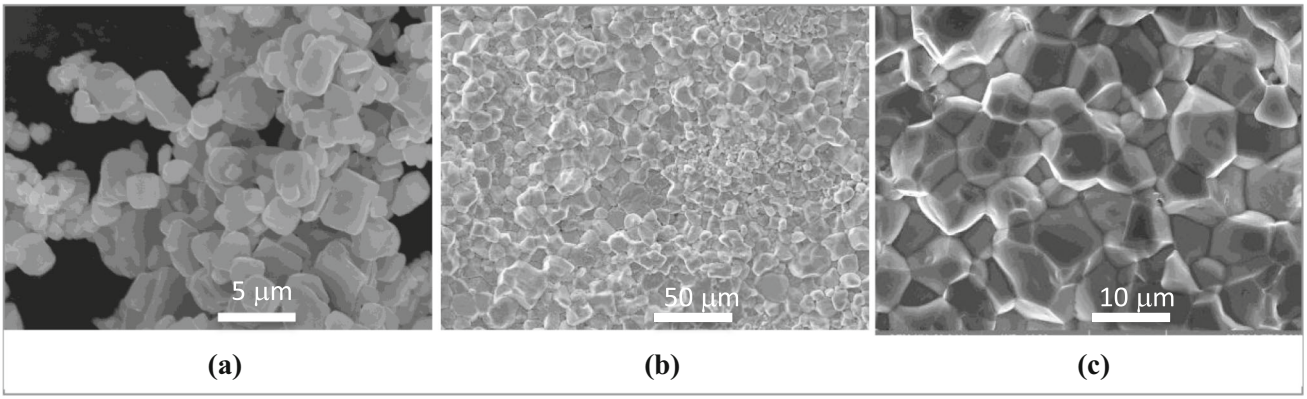

Fig. 4 SEM microstructures of **a** the synthesized powders with in-beam SE detector, **b** and **c** the fractured surface of the SPS sintered ceramic at two different magnifications, with SE detector

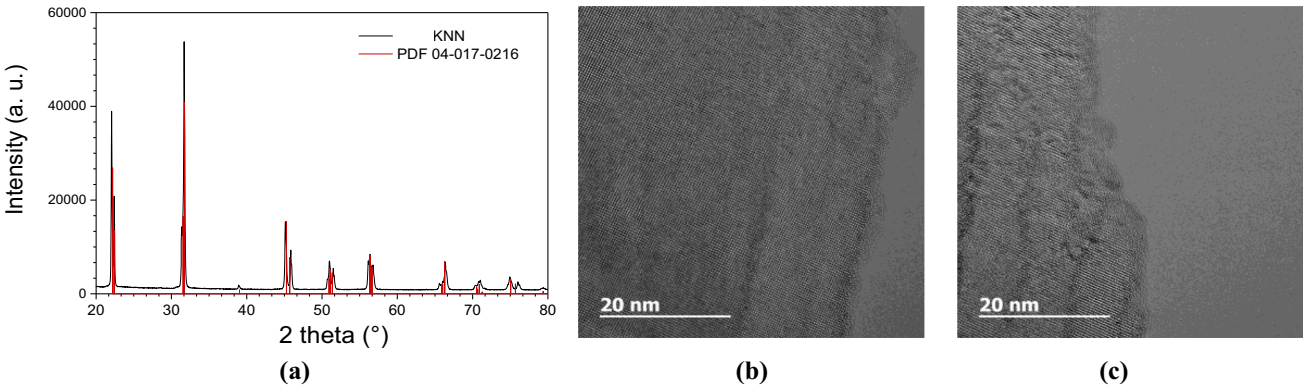

Fig. 5 **a** XRD diffractogram of the synthesized KNN powder and TEM images of the contrast observed at the edges of the grains, with **b** the majority of highly crystalline, defects-free grains and **c** some disturbed contrasts observed in rare grains, probably due to less crystallized areas caused by possible composition fluctuations or other structural defects

In raw SPS ceramics, a high density of defects is present corresponding to a disturbed contrast in the whole grain (Fig. 6a). The high heating and cooling rates, coupled with the uniaxial pressure submitted to the grains during the SPS run can easily explain the presence of a high density of dislocations, born during the high temperature creep of the matter, and leading to rapid diffusion paths and complete densification.

The second point is the presence of amorphous carbon clearly observed around the grains in raw SPS KNN, with a regular layer of a few nanometers (Fig. 6b). The carbon detected here is amorphous and not crystallized; it can suggest that it is only carbon which was embedded during the packing of the powder and that cannot escape like in conventional sintering because of the confined environment of the SPS process and the presence of carbon all around. The lack of oxygen prevents it to transform in CO_2 but it does not diffuse inside the grains, as observed in spinel or alumina ceramics sintered by SPS [36,37], because of the rather low temperatures, below 1000°C, used for KNN sintering.

After annealing for 2 h at 900°C, under oxygen flow, Fig. 6b, c shows much lower defects density with a soft, regular and undisturbed contrast and no more carbon around the grains.

TEM observations were completed by UV–visible, Raman and fluorescence measurements on raw and annealed samples. First of all, any of these techniques can make a difference between the two faces of the ceramic pellets; this indicates that, at this scale of observation, the homogeneity of the ceramics is guaranteed.

The Raman spectra registered in different parts of the same sample surface and obtained for the raw and annealed ceramics (Fig. 7a, b), are the signature of the orthorhombic phase of the KNN compound. They confirmed XRD analyses (not shown here). These spectra show slight differences which underline chemical inhomogeneities, that can be the signature of a slightly different chemical composition from one area to another. The reducing atmosphere during the SPS tests suggest that these deviations are related to O vacancies that might be balanced by Na, K removal, or niobium valence modifications.

However, since the spectra of the two samples show globally the same Raman modes and similar spectra, it can be considered that the two samples do not show any real structural difference and are therefore identical.

The photoluminescence spectra show a large difference between the raw and annealed samples (Fig. 7c, d). Indeed, the spectra of the raw sample show two

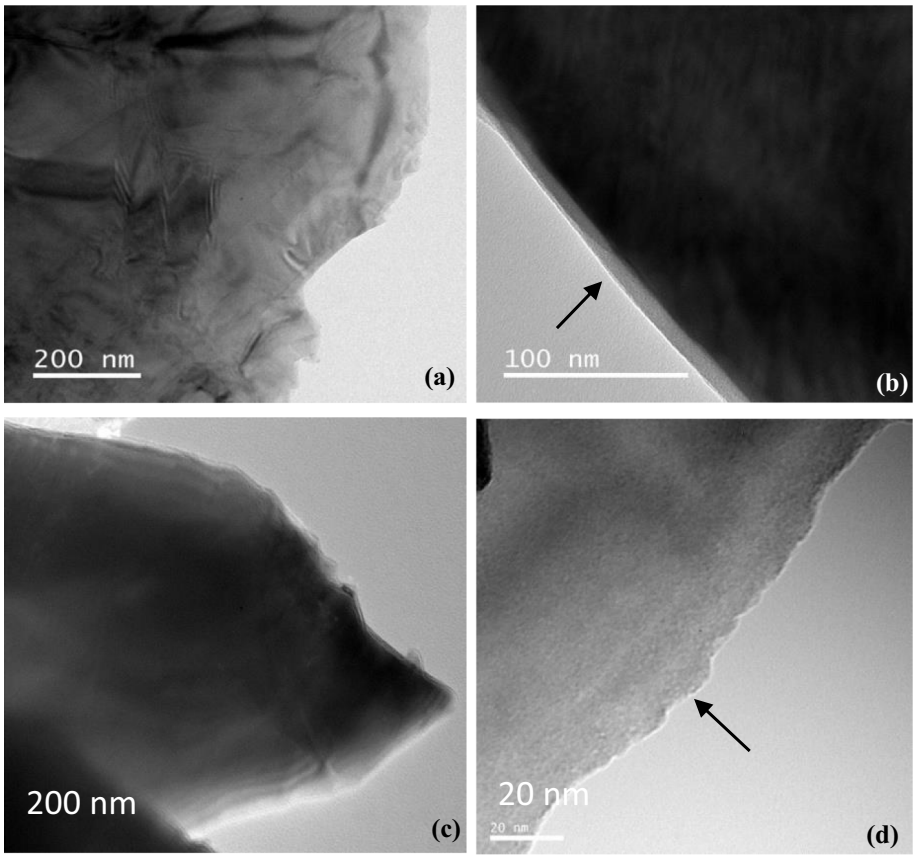

Fig. 6 Typical TEM contrasts insides the grains for raw **a** and oxygen annealed **c** SPS ceramics. Black arrow in raw sample **b** highlights carbon amorphous layer at the edge of grains, and black arrow in annealed sample **d** indicates that the that carbon layer is not anymore found around the grains

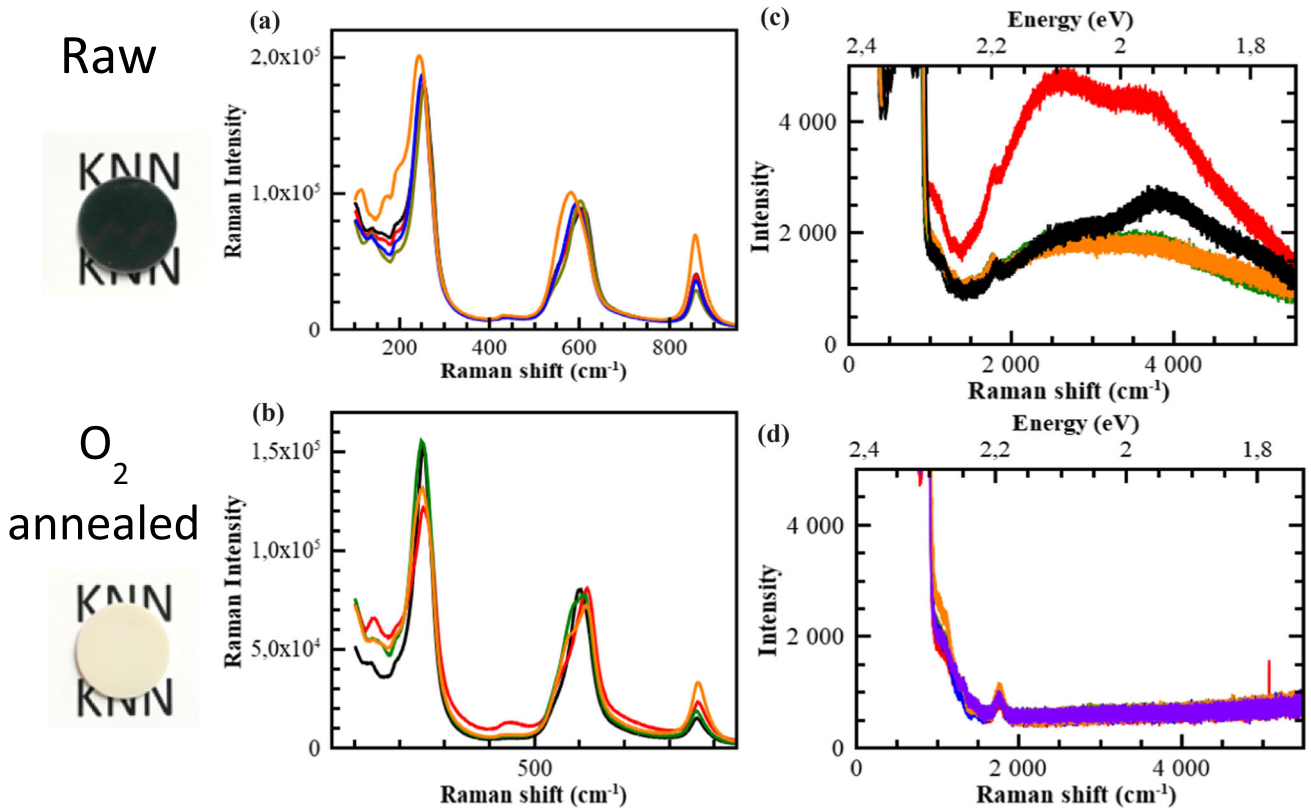

Fig. 7 Raman (**a**, **b**) and photoluminescence (**c**, **d**) spectra of raw and oxygen annealed KNN ceramics using an excitation 514 nm

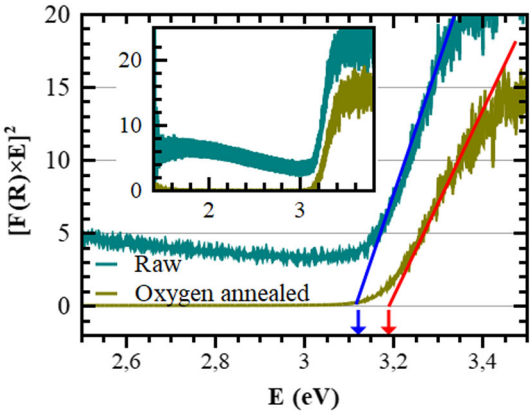

Fig. 8 Tauc plots obtained from diffuse reflectance spectra of raw and oxygen annealed KNN samples

peaks at about 1.9 eV and 2.1 eV. Otherwise, UV-visible spectroscopy showed a gap of about 3.1–3.2 eV for both samples (Fig. 8) in agreement with the values reported for KNN ceramics [53–55]. This demonstrates the modification of electronic structure of the raw sample and existence of electronic states in the gap. The presence of these levels can be explained by the presence of chemical defects (sodium, potassium or oxygen). However, the sample having undergone annealing under oxygen does not present such transitions, which rules out the hypothesis of sodium or potassium non stoichiometry that cannot be recovered by annealing. It is, therefore, concluded that these levels are the signature of the presence of oxygen defects in the raw sample, which are completely fulfilled with oxygen annealing. As it was observed for the oxygen-deficient $KTaO_3$, peaks observed at 1.9 eV and 2.1 eV could be attributed to transitions between self-trapped electron/hole states and valence/conduction bands [56].

As far as we can believe in EDX analysis and its precision commonly known at 2 at. %, and without considering the oxygen atomic ratio that is not correctly measured by this technique due to its low atomic number, the result of the cationic analyses indicates $K_{0.495}Na_{0.495}Nb_1O_x$ to $K_{0.52}Na_{0.48}Nb_1O_x$, rather close to the nominal $K_{0.5}Na_{0.5}Nb_1O_x$ composition, which confirm the composition homogeneity observed and that the conditions of SPS sintering are able to avoid the alkali volatilization.

3.4 Piezoelectric properties

The important point of this study is to consider if spark plasma sintered KNN ceramics, followed by oxygen annealing, are able to lead to good piezoelectric properties, in order to replace (Pb,Zr) TiO_3 by lead-free soft piezoceramics in devices such as transducers. Table 1 compares the material characteristics and the electromechanical constants obtained from KNN ceramics with conventional sintering at 1110°C, for 10 hours, and from ceramics of the present study, sintered at 920°C, under 50 MPa with 10 mins dwell at high temperature. To catch the functional properties of the piezoelectric ceramics, it must be underlined that the fitting process is made on the thickness mode signal of the impedance, and the electrical losses and quality factor are calculated from this signal.

The results presented in Table 1 clearly show several benefits of spark plasma sintering, which lead to dense ceramics with a smaller grain size and an improvement of all the dielectric and piezoelectric characteristics.

These results are significant and can solve most of the drawbacks of KNN sintering, which can be reproducibly produced without any sintering aid, and without any incidence on the cations introduction in the crystal structure and charge balance discussed in many studies with versatile results.

To complete the effect of the spark plasma sintering on KNN ceramics preparation, the influence of the pressure applied during the run is studied. This is one of the main parameters that can be varied in SPS process, and the effect on the piezoelectric properties has to be controlled before further investigations of the KNN system. The pressure was varied from 25 to 150 MPa without modifications of the thermal cycle. First of all, the ceramic microstructures exhibit the same average grain size whatever the applied pressure. Figure 9 shows that in spite of an increase of the relative density from 97 to 98.5% by applying a higher pressure, the resulting electromechanical coefficients k_p and k_t do not change significantly, with less than 10% variations. This means that over 96% relative density, the SPS pressure does not influence the electromechanical coupling factors. To sum up the results, this study proves that SPS technique is able to achieve reproducible and improved characteristics of KNN piezoelectric ceramics compared to conventional sintering.

4 Conclusion

As conclusion, spark plasma sintering technique is promising to get high densification over 97% in KNN system and to prevent alkali volatilization in order to control the nominal composition of KNN ceramics. However, dislocations and oxygen vacancies are introduced by SPS but they can be easily removed and oxygen completely recovered respectively, by 2 hours post annealing treatment under oxygen at 900°C. Moreover, the functional piezoelectric properties are sensitively improved, certainly thanks to the density and homogeneity improvements, without any doping.

With such an efficient processing, it will thus be possible to focus only on the creation of morphotropic phase boundaries and morphotropic phase transitions to control piezoelectric domains and polarization stiffness of KNN system, to get piezoelectric properties competitive and in the race of PZT alternative solution.

Some industries are already ready to produce samples by SPS, because of the geometrical accuracy (diameter and thickness can be obtained without further polishing

Table 1 Relative densities and mean grains size of the ceramic with dielectric and electromechanical constants extracted from the complex electrical impedance measurement, fit with KLM model [46]

Sintering conditions	Relative density (%)	Mean grain size (μm)	$\varepsilon^{T}_{r,33}$	k_t (%)	k_p (%)	δ_e (%)	δ_m (%)	Z (MRay)
Conventional sintering 1110°C / 10 h [13]	90–92	8–10	200	25–35	30–35	5	5–10	23
KNN–SPS (10 samples) 920°C /50 MPa/10 min	97–98	5	330	27–30	45-50	3	2–4	28–30

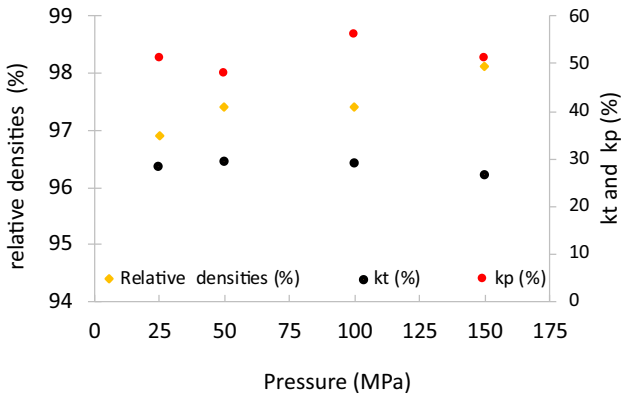

Fig. 9 Overview of the relative densities, k_p, k_t electromechanical coefficients evolution with different pressures applied during spark plasma sintering

or cutting process), the quality and the homogeneity of the microstructure, and the possibility to keep nanostructured materials [57].

The next step for industrial transfer of SPS technique and lead-free transducers production is to study the upscaling of this process and the resulting piezoelectric properties, that might be very useful to prepare low costs elements of transducers.

Acknowledgements The authors are grateful to the French METSA network (FR3507) for the financial support of the Transmission Electron Microscope experiment, and to T. Chartier (GREMAN, IUT Blois) for DTA–TGA measurements.

References

1. B. Jaffe, *Piezoelectric Ceramics*, Academic Press (London, 1971)
2. EU-Directive 2002/95/EC: RoHS, Off. J. Eur. Union, 46(L37) 19 (2003)
3. S. Zhang, R. Xia, T.R. Shrout, J. Electroceram. **19**, 251 (2007)
4. H.-C. Thong, C. Zhao, Z. Zhou, C.-F. Wu, Y.-X. Liu, Z.-Z. Du, J.-F. Li, W. Gong, K. Wang, Mater. Today **29**, 37 (2019)
5. J. Rödel, W. Jo, K.T.P. Seifert, E.-M. Anton, T. Granzow, D. Damjanovic, J. Am. Ceram. Soc. **92**, 1153 (2009)
6. J. Wu, D. Xiao, J. Zhu, Chem. Rev. **115**, 2559 (2015)
7. C.-H. Hong, H.-P. Kim, B.-Y. Choi, H.-S. Han, J.S. Son, C.W. Ahn, W. Jo, J. Materiom. **2**, 1 (2016)
8. J. Rödel, J.-F. Li, MRS Bull. **43**, 576 (2018)
9. L. Egerton, D.M. Dillon, J. Am. Ceram. Soc. **42**, 438 (1959)
10. B. Malič, Acta Chim. Slov. **55**, 719 (2008)
11. H. Jiang, T.T. Su, H. Gong, Y.C. Zhai, Cryst. Res. Technol. **46**, 85 (2011)
12. B. Malič, J. Koruza, J. Hreščak, J. Bernard, K. Wang, J. Fisher, A. Benčan, Materials **8**, 8117 (2015)
13. M. Bah, F. Giovannelli, F. Schoenstein, G. Feuillard, E. Le Clezio, I. Monot-Laffez, AIP Conf. Proc. **1627**, 3 (2014)
14. M. Bah, F. Giovannelli, R. Retoux, J. Bustillo, E.L. Clezio, I. Monot-Laffez, Cryst. Growth Des. **16**, 315 (2016)
15. J. Koruza, H. Liu, M. Höfling, M.-H. Zhang, P. Veber, J. Mater. Res. **35**, 990 (2020)
16. Y. Saito, H. Takao, T. Tani, T. Nonoyama, K. Takatori, T. Homma, T. Nagaya, M. Nakamura, Nature **432**, 84 (2004)
17. L. Jiang, J. Xing, Z. Tan, J. Wu, Q. Chen, D. Xiao, J. Zhu, J. Mater. Sci. **51**, 4963 (2016)
18. D. Lin, K.W. Kwok, H. Tian, H.W.L. Chan, J. Am. Ceram. Soc. **90**, 1458 (2007)
19. V. P, R. Jose, K. V. Saravanan, RSC Adv. **9**, 34888 (2019)
20. L. Wang, W. Ren, P.C. Goh, K. Yao, P. Shi, X. Wu, X. Yao, Thin Solid Films **537**, 65 (2013)
21. M.-S. Chae, J.-H. Koh, S.-K. Lee, J. Alloys Compd. **587**, 729 (2014)
22. Y.G. Lv, C.L. Wang, J.L. Zhang, L. Wu, M.L. Zhao, J.P. Xu, Mater. Res. Bull. **44**, 284 (2009)
23. D. Lin, Z. Li, S. Zhang, Z. Xu, X. Yao, J. Am. Ceram. Soc. **93**, 941 (2010)
24. F. Jean, F. Schoenstein, M. Zaghrioui, M. Bah, P. Marchet, J. Bustillo, F. Giovannelli, I. Monot-Laffez, Ceram. Int. **44**, 9463 (2018)
25. G.-Z. Zang, X.-J. Yi, J. Du, Y.-F. Wang, Mater. Lett. **64**, 1394 (2010)
26. Y.S. Sung, Appl. Phys. Lett. **105**, 142903 (2014)
27. J. Koruza, A.J. Bell, T. Frömling, K.G. Webber, K. Wang, J. Rödel, J. Materiom. **4**, 13 (2018)
28. S. Garroni, N. Senes, A. Iacomini, S. Enzo, G. Mulas, L. Pardo, S. Cuesta-Lopez, Phys. Status Solidi A **215**, 1700896 (2018)

29. T. Zheng, J. Wu, D. Xiao, J. Zhu, Prog. Mater. Sci. **98**, 552 (2018)
30. H. Thong, Z. Xu, C. Zhao, L. Lou, S. Chen, S. Zuo, J. Li, and K. Wang, J. Am. Ceram. Soc. JACE. 16070 (2018)
31. J.-F. Li, Y. Zhen, B.-P. Zhang, L.-M. Zhang, K. Wang, Ceram. Int. **34**, 783 (2008)
32. N. Liu, K. Wang, J.-F. Li, Z. Liu, J. Am. Ceram. Soc. **92**, 1884 (2009)
33. M. Bah, F. Giovannelli, F. Schoenstein, G. Feuillard, E. Le Clezio, I. Monot-Laffez, Ceram. Int. **40**, 7473 (2014)
34. G. Corapcioglu, M. A. Gulgun, K. Kisslinger, S. Sturm, Shikhar. K. Jha, R. Raj, J. Ceram. Soc. Jpn. **124**, 321 (2016)
35. R. Pinho, A. Tkach, S. Zlotnik, M.E. Costa, J. Noudem, I.M. Reaney, P.M. Vilarinho, Appl. Mater. Today **19**, 100566 (2020)
36. M. Michálek, M. Michálková, G. Blugan, J. Kuebler, J. Eur. Ceram. Soc. **38**, 193 (2018)
37. K. Morita, B.-N. Kim, H. Yoshida, K. Hiraga, Y. Sakka, J. Eur. Ceram. Soc. **38**, 2588 (2018)
38. Y. Kizaki, Y. Noguchi, M. Miyayama, Appl. Phys. Lett. **89**, 142910 (2006)
39. G. Bernard-Granger, N. Benameur, A. Addad, M. Nygren, C. Guizard, S. Deville, J. Mater. Res. **24**, 2011 (2009)
40. G. Bernard-Granger, A. Néri, C. Navone, M. Soulier, J. Simon, M. Marinova-Atanassova, J. Mater. Sci. **47**, 4313 (2012)
41. J.G. Fisher, S.-J.L. Kang, J. Eur. Ceram. Soc. **29**, 2581 (2009)
42. R. Cong, G. Qiu, C. Yue, M. Guo, F. Cheng, M. Zhang, Ceram. Int. **44**, 19764 (2018)
43. M.I. Morozov, H. Kungl, M.J. Hoffmann, Appl. Phys. Lett. **98**, 132908 (2011)
44. W.E. Vargas, G.A. Niklasson, Appl. Opt. **36**, 5580 (1997)
45. L.-P. Tran Huu Hue, Ultrasonics 219 (2000)
46. R. Krimholtz, D.A. Leedom, G.L. Matthaei, Electron. Lett. **6**, 398 (1970)
47. Int. J. M Aterials Chem. 5 (2013)
48. R. Wang, R. Xie, T. Sekiya, Y. Shimojo, Mater. Res. Bull. **39**, 1709 (2004)
49. J.-F. Li, K. Wang, B.-P. Zhang, L.-M. Zhang, J. Am. Ceram. Soc. **89**, 706 (2006)
50. B.-P. Zhang, J.-F. Li, K. Wang, H. Zhang, J. Am. Ceram. Soc. **89**, 1605 (2006)
51. F. Delorme, M. Bah, F. Schoenstein, F. Jean, M. Zouaoui Jabli, I. Monot-Laffez, F. Giovannelli, Mater. Lett. **162**, 24 (2016)
52. D. Kuscer, A. Kocjan, M. Majcen, A. Meden, K. Radan, J. Kovač, B. Malič, Ceram. Int. **45**, 10429 (2019)
53. M. Lun, X. Zhou, S. Hu, Y. Hong, B. Wang, A. Yao, W. Li, B. Chu, Q. He, J. Cheng, Y. Wang, Ceram. Int. **47**, 28797 (2021)
54. S. Kumar, M. Shandilya, S. Thakur, N. Thakur, J. Sol. Gel Sci. Technol. **88**, 646 (2018)
55. K. Shalini, D. Prabhu, N.V. Giridharan, Appl. Phys. A **124**, 866 (2018)
56. S.K. Ojha, S.K. Gogoi, P. Mandal, S.D. Kaushik, J.W. Freeland, M. Jain, S. Middey, Phys. Rev. B **103**, 085120 (2021)
57. F. Delorme, R. Dujardin, F. Schoenstein, B. Pintault, P. Belleville, C. Autret, I. Monot-Laffez, F. Giovannelli, Ceram. Int. **45**, 8313 (2019)